

www.acsanm.org Article

Influence of Pd Concentration in Au-Pd Nanoparticles for the **Hydrogenation of Alkynes**

Alexandre C. Foucher, Hio Tong Ngan, Tanya Shirman, Amanda Filie, Kaining Duanmu, Michael Aizenberg, Robert J. Madix, Cynthia M. Friend, Joanna Aizenberg, Philippe Sautet, and Eric A. Stach*



Cite This: ACS Appl. Nano Mater. 2023, 6, 22927-22938



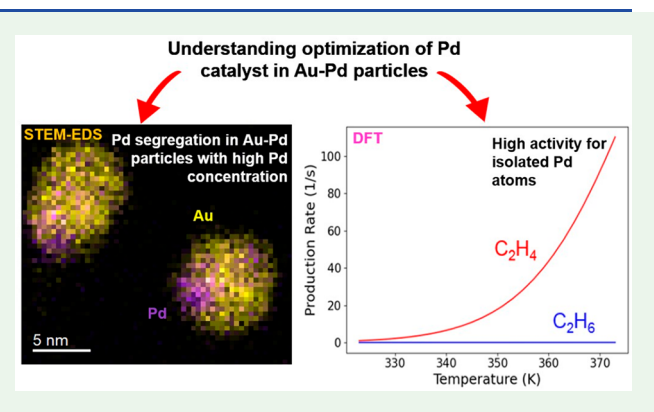
ACCESS

Metrics & More

Article Recommendations

Supporting Information

ABSTRACT: Supported Au—Pd nanoparticles with low Pd content (between 2% and 25%) are excellent catalysts for the selective hydrogenation of alkynes into alkenes, a crucial step for elimination of alkynes from the reactants for olefin polymerization. They have better selectivity at high conversions for the hydrogenation of 1hexyne to 1-hexene compared to that of pure Pd. However, the role of Pd concentration in Au-Pd particles in maximizing the activity per gram of Pd remains elusive. This work combines scanning transmission electron microscopy (STEM) and density functional theory (DFT) to determine how Pd concentration in the dilute limit affects the activity and selectivity of Au-Pd particles for the hydrogenation of acetylene. Atomic resolution microscopy shows increased Pd segregation to the surface with increasing Pd



concentration (above 9%), and DFT analysis shows that isolated Pd atoms on the Au-Pd surface are highly active for acetylene hydrogenation compared to Pd atoms adjacent to other Pd atoms. A high concentration of isolated and active Pd atoms combined with increased segregation of Pd toward the surface explains the existence of an optimum for catalytic properties. It explains the high performance of Au_{0.96}Pd_{0.04} compared to Au-Pd particles with lower or higher Pd concentrations.

KEYWORDS: Catalysis, alkyne hydrogenation, PdAu nanocatalysts, STEM, DFT, microkinetic simulation, optimization of Pd

INTRODUCTION

Bimetallic nanoparticles are an emerging class of materials and are becoming of great interest in the field of heterogeneous catalysis. For instance, Pd is an excellent catalyst for a large range of reactions, and its performance can be boosted by alloying it with another transition metal.^{1,2} AuPd alloys are critical catalysts for reactions such as the oxidation of alcohols, the electrochemical reduction of $CO_{24}^{\ \ 4}$ and the electrocatalytic production of hydrogen peroxide (H2O2).5 One of the most common application of AuPd systems is for the hydrogenation of alkynes (C \equiv C) into alkenes (C \equiv C). 6-9 Control over the structure of AuPd particles greatly influences their stability, activity, and selectivity. 10,11 Previous publications have shown that AuPd particles, in the dilute Pd range with Pd concentration between 2% and 9%, supported on raspberry colloid-templated (RCT)-SiO₂ have particularly useful catalytic properties. 12-16 This synthesis approach improves the stability of the nanoparticles at elevated temperature by preventing particle migration and coalescence (PMC) and substantial changes in morphology during pretreatment. 12,17-19

Prior studies have also shown that the highest rate for 1hexyne conversion was achieved with Pd_{0.04}Au_{0.96} particles.^{20,6} In contrast, $Pd_{0.02}Au_{0.98}$ and $Pd_{0.09}Au_{0.91}$ were less efficient, as the conversion of 1-hexyne per atom of Pd was markedly lower than that for the Pd_{0.04}Au_{0.96} particles. 6 The system and previous results are summarized in Figure 1. A schematic of the fabrication process is shown in Figure 1a, and details about the synthesis process can be found in previous publications. 6,14,21 The existence of an optimum at 4 atomic % of Pd indicates that the Pd concentration plays a crucial role.²² This could be due to surface structure modification or the elements' spatial distribution when the Au:Pd ratio is modified. Indeed, it has been shown that small Au particles have an icosahedral form with predominant {111} surfaces.²³⁻²⁷ However, the effect of the concentration of Pd on the shape and surface structure of Au-Pd particles is not known and could explain the difference in properties: a modification of the surface can cause

September 7, 2023 Received: Revised: November 2, 2023 Accepted: November 3, 2023 Published: December 7, 2023





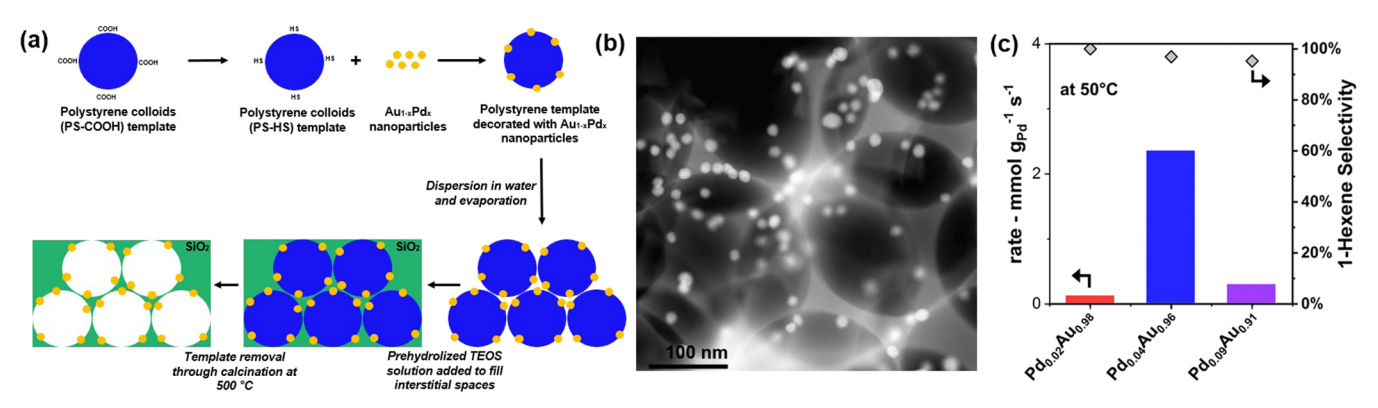


Figure 1. Catalytic system studied in this work. (a) Fabrication process of the sample. Gold nanoparticles are embedded in porous SiO₂ (obtained with tetraethyl orthosilicate, i.e., TEOS) using a sacrificial polystyrene template. 14 (b) High-angle annular dark-field (HAADF)-STEM image of particles on the porous SiO₂. (c) Measurements of the rate of 1-hexyne conversion (bars) and selectivity (gray diamonds) for 1-hexene production. An optimum in the rate of 1-hexyne conversion is achieved for Au_{0.96}Pd_{0.04}. Reproduced from ref 6. Copyright 2020 American Chemical Society.

substantial changes in the electronic structure at the surface of the catalysts. $^{28-30}$ This change in electronic structure subsequently alters gaseous molecules' adsorption and desorption energies and ultimately determines the yield of the desired product in the reaction.³¹ Additionally, the spatial distribution of Pd in Au-Pd particles has not been investigated. It is known that a high concentration of Pd in Au-Pd particles causes the formation of Pd-rich islands on the surface of the particles, 32 but the prevalence and size of these Pd-rich islands were not correlated with the concentration of Pd. Aside from changes in activity as a function of Pd concentration, high selectivity for Pd_{0.02}Au_{0.98}, Pd_{0.04}Au_{0.96}, and Pd_{0.09}Au_{0.91} was also observed (close to 100% for the three samples), but the origin of this has not been fully understood.³³ Thus, this investigation focuses on the variations of activity and selectivity observed for the catalysts containing Au_{1-x}Pd_x particles with changes in Pd concentrations.

This work aims to answer why a concentration of Pd of 4 at % is optimal in the alloy for alkyne hydrogenation and to explain the observed high selectivity for low Pd concentration. By combining scanning transmission electron microscopy (STEM) measurements and density functional theory (DFT), we link the distribution of Pd atoms on the surface of dilute Au-Pd particles and their catalytic performance. STEM was combined with energy-dispersive X-ray spectroscopy (EDS) to investigate the morphology and composition of Au-Pd particles on the nanoscale. Four Au-Pd alloys were characterized with STEM: $Pd_{0.25}Au_{0.75}$, $Pd_{0.09}Au_{0.91}$, Pd_{0.04}Au_{0.96}, and Pd_{0.02}Au_{0.98}. DFT analysis shows that Pd monomers, dimers, and trimers on the {111} surfaces do not have the same activity for the hydrogenation of acetylene in ethylene. The samples were investigated before exposure to alkynes and after calcination at 500 °C in air for 2 h, as described in our previous work.⁶ The calcination process removes all of the organic residues.

MATERIALS AND METHODS

Catalyst Preparation. The preparation of PdAu nanoparticles on RCT has been reported in previous publications. 34,35 Composite colloids were synthesized by adding $\mathrm{Pd_xAu_{1-x}}$ nanoparticles to a colloidal dispersion of thiol-modified polystyrene colloids. The interstitial space of the dry crystal assembly was then filled with a sol–gel silica precursor. The infiltrated colloidal crystal assembly was then calcinated at 500 °C for 2 h to remove the polymer and produce a porous matrix of $\mathrm{SiO_2}$ with partially embedded $\mathrm{Pd_xAu_{1-x}}$ particles. All catalysts in this work were prepared in this manner.

Scanning Transmission Electron Microscopy. Images and EDS data were collected with a JEOL NEOARM instrument operated at 200 kV in scanning transmission electron microscopy (STEM) mode. The sample was first ground and diluted in isopropanol. A drop of the suspension was then deposited on lacey carbon films on copper grids (Electron Microscopy Science).

For imaging and EDS analysis, the probe current was 150 pA, the condenser lens aperture was 40 μ m, the convergence angle was 27 mrad, and the camera length was 4 cm. Two JEOL EDS detectors above the sample collected fluorescent X-rays. The images were displayed with DigitalMicrograph, software provided by Gatan Inc. For electron energy-loss spectroscopy (EELS), the same probe current and condenser lens aperture were used as for EDS, except that the camera length was 2 cm. A Gatan imaging filter (GIF) of 5 mm was used, and the EELS data were obtained with a K2-IS camera.

DFT Calculations. All DFT calculations were performed with the Vienna ab initio simulation package (VASP). The surfaces of Pd/ Au(111) for acetylene hydrogenation were modeled using a 6-layer slab and a (3×3) unit cell, while a (4×4) unit cell was used instead for 1-hexyne hydrogenation. The dDsC-dispersion-corrected PBE functional, 38,39 a cutoff energy of 400 eV, and a Monkhorst–Packgenerated $7 \times 7 \times 1$ K-points mesh were employed for all calculations. 40 During structural optimization, the bottom four layers of the slab were fixed at the bulk Au lattice parameters, while the upper two layers and the adsorbates were allowed to relax until convergence thresholds of 10⁻⁵ eV for energies and 0.03 eV/Å for forces were reached. A stricter energy convergence criterion of 10-7 eV was set for the transition states. Transition states were located using both the climbing image nudged elastic band (CI-NEB)⁴¹ and the dimer method. 42 For simplicity, free energy calculations neglect zero-point energies and vibrational entropies of both the surface and gaseous species. All atomic configurations reported were visualized using VESTA.4

Microkinetic Simulations. Microkinetic simulations were performed by using the energetics obtained from DFT calculations. Collision theory (eqs 1 and 2) and transition state theory (eq 3) were used to compute the rate constants for adsorption $(k_{ads,i})/desorption$ $(k_{des,i})$ and surface reactions (k_i) , respectively:

$$k_{\mathrm{ads},i} = \frac{A_{\mathrm{st}}}{\sqrt{2\pi m_i k_{\mathrm{B}} T}} \tag{1}$$

$$k_{\mathrm{des},i} = k_{\mathrm{ads},i} P^{\mathrm{o}} \exp \left(\frac{\Delta G_{\mathrm{ads},i}^{\mathrm{o}}}{k_{\mathrm{B}} T} \right)$$
 (2)

$$k_{j} = \frac{k_{\rm B}T}{h} \, \exp\!\left(-\frac{\Delta H^{\ddagger}}{k_{\rm B}T}\right) \exp\!\left(\frac{T\Delta S^{\ddagger}}{k_{\rm B}T}\right) \tag{3}$$

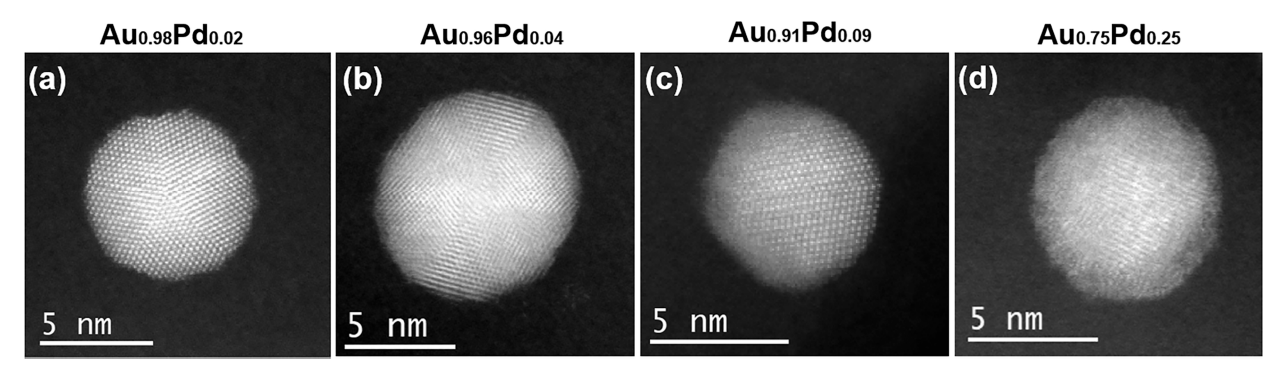


Figure 2. Increasing the Pd content modifies the morphology of $Au_{1-x}Pd_x$ particles. (a) $Au_{0.98}Pd_{0.02}$ particles have an icosahedral shape. (b) An $Au_{0.96}Pd_{0.04}$ icosahedron, although the surface does not appear as flat as in (a). (c) $Au_{0.91}Pd_{0.09}$ particles with sharp edges on the right and a rough surface on the left. The inclusion of Pd atoms in the Au crystal lowered the surface energy, destabilizing the {111} facets in some parts of the particles. (d) $Au_{0.75}Pd_{0.25}$ with no indication of a regular polyhedron. Surfaces are irregular due to the modification of surface energies with an increased Pd concentration. Additional STEM images are provided in Figures S2 and S3.

where $A_{\rm st}$ is the area of the adsorption site, m_i is the mass of the adsorbing species i, $k_{\rm B}$ is the Boltzmann's constant, T is the temperature, P° is the standard state pressure, $\Delta G_{{\rm ads},i}^{\circ}$ is the adsorption free energy of species i under standard state pressure, h is the Planck's constant, and ΔH^{\ddagger} and ΔS^{\ddagger} are, respectively, the enthalpy and entropy difference between the initial state and the transition state in elementary step j.

In the microkinetic simulations, species rate equation i was obtained from the combination of the rate equation of each elementary step j:

$$\frac{\mathrm{d}\theta_i}{\mathrm{d}t} = \sum_j \nu_{ij} r_j \tag{4}$$

where θ_i is the surface coverage of species i, t is time, ν_{ij} is the stoichiometric coefficient of species i in step j, and r_j is the reaction rate of elementary step j.

The catalyst surface is set to be bare initially. Solutions are then obtained from the set of differential equations (see Tables S1, S2, and S3) when the system reaches steady state (i.e., $\frac{\mathrm{d}\theta_i}{\mathrm{d}t}=0$), which is safely assumed to occur before t=50 s.

The degree of rate and selectivity controls (DRCs and DSCs, respectively) measure the extent of an increase in the net reaction rate and the selectivity with an increase in the rate constant of a specific elementary step, which could be reflected in the free energy of the transition state. In such calculations, the free energies of all of the other transition states and surface intermediates are kept constant. Mathematically, DRCs and DSCs are defined as

$$DRC = \left(\frac{\partial \ln(r)}{\partial \left(\frac{-G_{j}^{o,TS}}{k_{B}T}\right)}\right)_{G_{j\neq k}^{o,TS}, G_{im}^{o}}$$
(5)

where r is the net reaction rate, S is the selectivity defined as the ratio of ethylene formation rate to acetylene consumption rate, $G_j^{o,TS}$ is the standard state free energy of the transition state of the elementary step j, and G_{im}^{o} is the standard state free energy of all surface intermediates.

■ RESULTS AND DISCUSSION

High-resolution STEM imaging was first performed on the four PdAu alloys to investigate their morphology. Results are summarized in Figure 2 and show a correlation between the shape and Pd content. When the Pd concentration is low, particles have sharp edges and facets typical of an icosahedral structure. By "sharp facets", we are referring to facets that do not have visible roughness or a curvy surface. This shape is

typical for pure Au particles, so one can conclude that a low concentration of Pd in an Au crystal does not modify the particle morphology in a significant way. In Figure 2a, it is possible to distinguish the facets of the Pd_{0.02}Au_{0.98} particles clearly. The sharp {111} facets expected for an icosahedral structure are present. In Figure 2b, the icosahedral morphology is broadly maintained as the Pd concentration is increased to 4%, albeit less strongly than that in Figure 2a. In Figure 2c, part of the particle has a rough surface, while other parts appear to be more ordered. To be clear, this is not an artifact of microscope focus due to the small depth of field: a through focal series did not make a difference. One can also hypothesize that the incorporation of Pd into Au increasingly changes the lattice parameter, destabilizing the energetic driving force that causes the formation of the icosahedral structure. 45-47 The trend is even more visible for Pd_{0.25}Au_{0.75} particles.

One can also point out the very rough surface of pure Pd particles, which supports our observation of increased surface roughness with Pd concentration (Figure S1). A broader investigation of large sets of particles shows that Au–Pd particles remain mostly faceted for a Pd concentration of up to 9%, as faceted surfaces are dominant in $Au_{0.98}Pd_{0.02}$, $Au_{0.96}Pd_{0.04}$, and $Au_{0.91}Pd_{0.09}$.

Table S4 provides the average particle sizes for the four groups of particles. A measurement conducted on 400 particles in each batch shows that the particle size is not correlated with the Pd atomic %. The average size ranged from 5.6 to 6.1 nm. Hence, changes in the morphology of $\mathrm{Au}_{1-x}\mathrm{Pd}_x$ particles are exclusively due to the Pd:Au ratio and not the size of the particles after synthesis.

An extensive EDS analysis was conducted on many particles to better understand the prevalence of heterogeneities. EDS maps were collected at the atomic scale to detect potential increases in the Pd concentration in the four samples. The results are summarized in Figures 3–5, which provide a visual understanding of the size and prevalence of compositional heterogeneities. This approach has been performed in previous work for other bimetallic particles 48,49 to avoid misleading conclusions by "cherry-picking" a single EDS map.

A short pixel time (0.05 s) was chosen to prevent beaminduced effects during spatial EDS acquisition, and the particles were not overexposed to the electron beam during STEM images. The shape of the particles was checked after acquisition to ensure that the beam did not induce structural

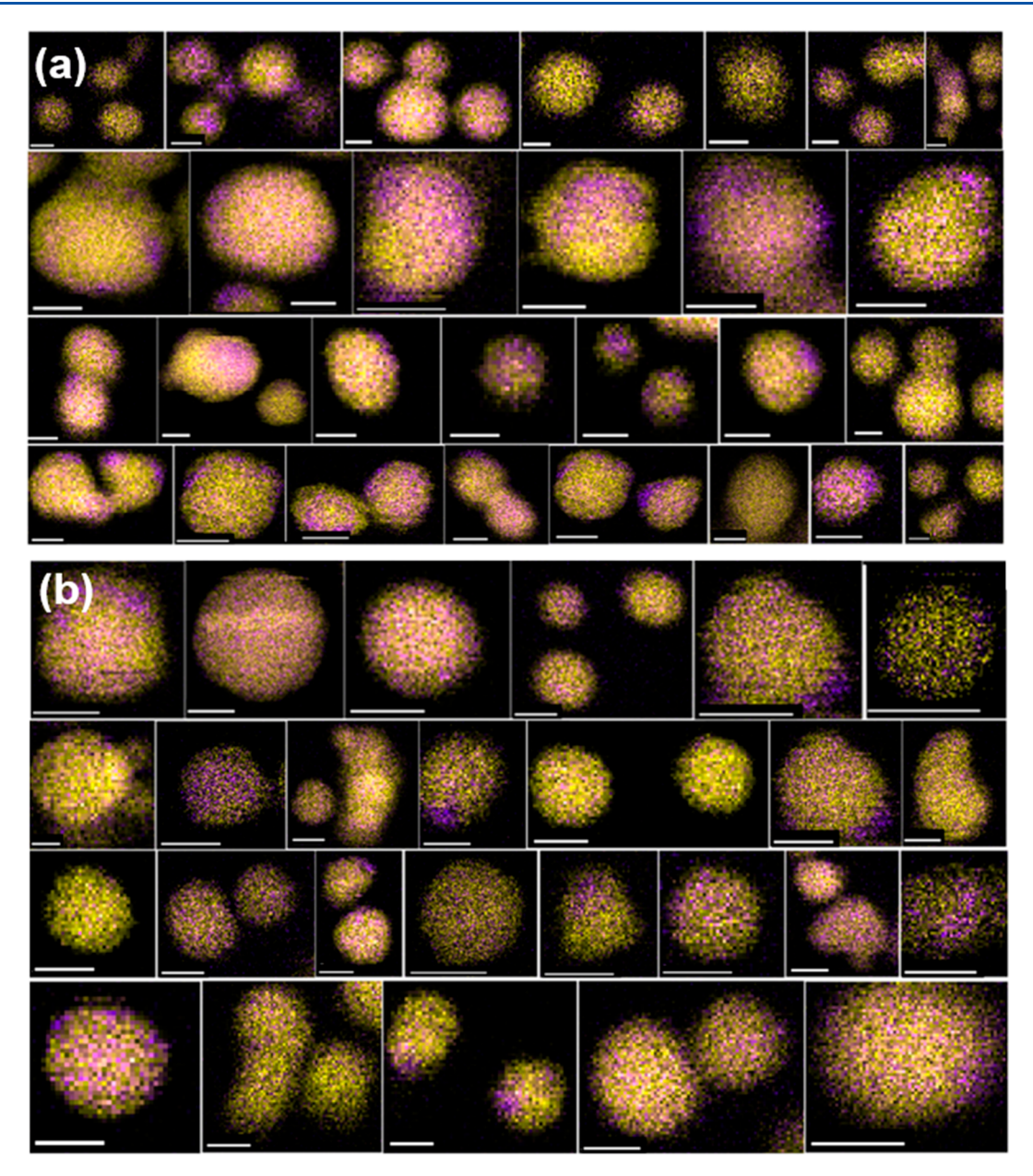


Figure 3. Collage of an ensemble of $Pd_{0.25}Au_{0.75}$ particles and $Pd_{0.09}Au_{0.91}$ analyzed with atomic-scale EDS maps. (a) Collage for $Pd_{0.25}Au_{0.75}$. (b) Collage for $Pd_{0.09}Au_{0.91}$. Pd-rich islands are frequently observed, which indicates that a high Pd concentration leads to coalescence of Pd-rich regions. All scale bars are 5 nm.

change during EDS scanning. We also know from previous experiments on these materials that Pd-rich islands are on the surface of the particles.³²

The conflated image in Figure 3a shows the distribution of Pd in a large set of Pd_{0.25}Au_{0.75} particles. It is possible to distinguish the presence of small Pd-rich islands frequently appearing in individual particles. A quantitative EDS analysis on these Pd-rich regions indicates that Pd content spikes to as high as 45%. EDS quantification on a series of EDS maps confirms that the average Pd concentration is 25%, which was also obtained with ICP-MS. Also, an XAS analysis in previous work about the same samples showed that Pd-rich islands are on the surface of the particles. Therefore, these Pd-rich regions will have an impact on the surface reaction and the catalytic properties of the sample.

The same approach was performed for Au_{0.91}Pd_{0.09} in Figure 3b and showed the presence of Pd-rich islands, although they appeared less frequently. A similar collage is provided for Au_{0.96}Pd_{0.04} (Figure 4a) and Au_{0.98}Pd_{0.02} (Figure 4b). In both of these more dilute cases, Pd-rich islands are nearly nonexistent. One can conclude that the Pd atomic concentration is directly correlated with the presence of Pd-rich regions: the higher the Pd content, the more likely it is to create a Pd-rich island. It should be emphasized that these islands are not pure Pd but rather regions with an increased Pd content. This is confirmed by the fact that the Au signal is also observed in these regions. Table S5 provides a statistical summary of the presence of Pd-rich islands and indicates a sharp increase in heterogeneities when the Pd content is above 4%. Hence, in $Au_{0.91}Pd_{0.09}$ and $Au_{0.75}Pd_{0.25}$ particles, many Pd atoms will remain within these Pd-rich islands. For

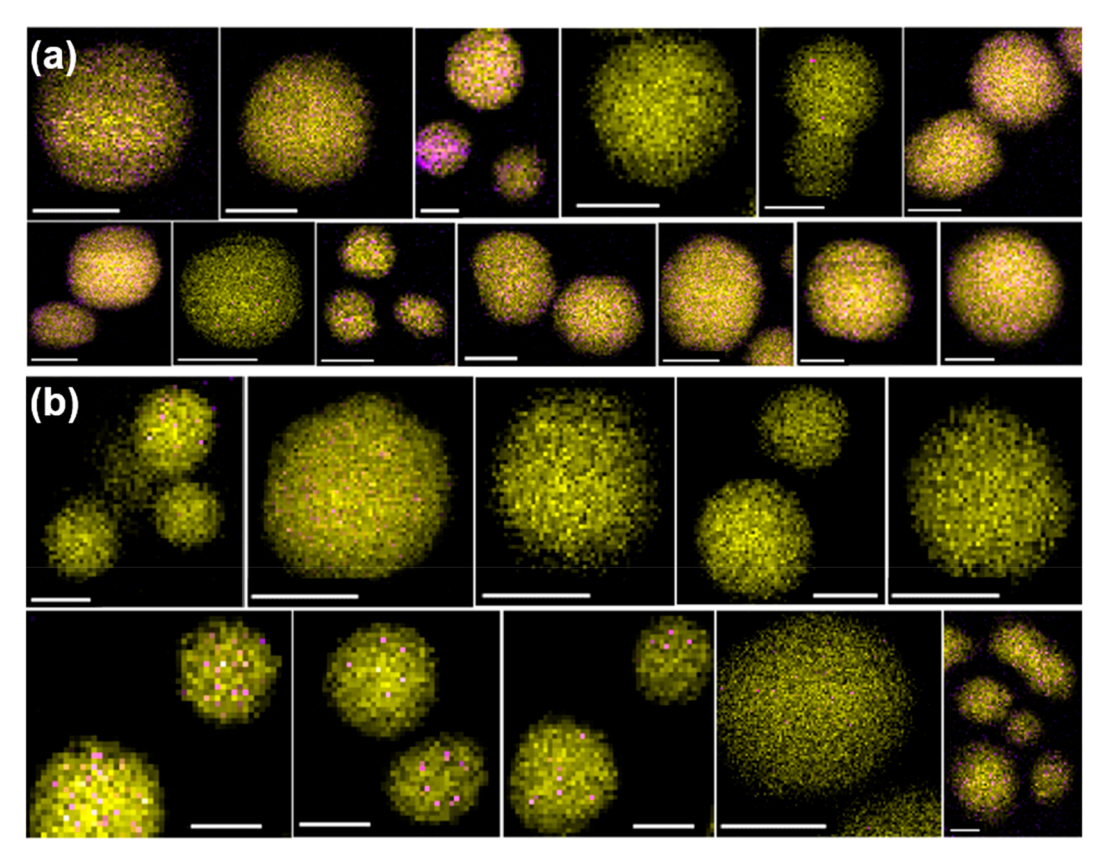


Figure 4. (a) Collage showing many EDS maps of Pd_{0.04}Au_{0.96} particles. Pd-rich islands within particles are nearly nonexistent. Pd heterogeneities appear as a factor explaining the increase of 1-hexyne conversion when the Pd atomic % is reduced from 9% to 4%. All scale bars represent 5 nm. (b) Collage showing many EDS maps of Pd_{0.02}Au_{0.98} particles. All scale bars represent 5 nm.

 $Au_{0.75}Pd_{0.25}/RCT$ -SiO₂, the probability of finding Pd-rich islands is 44.5%. It drops to 18.3% for $Au_{0.91}Pd_{0.09}$, 4% for $Au_{0.96}Pd_{0.04}$, and 0% for $Au_{0.98}Pd_{0.02}$.

It should also be noted that the SiO_2 support does not seem to play a role in the distribution and location of compositional heterogeneities within particles. EDS analysis of particles on SiO_2 edges did not reveal preferential coalescence of Pd at the $SiO_2/PdAu$ interface nor an increased Au concentration compared to the rest of the alloy. Also, based on the STEM-EDS data, we did not see any correlation between composition/heterogeneities and size of particles.

While the presence of Pd-rich islands for $Au_{0.91}Pd_{0.09}$ particles could explain their poor conversion rate, the origin of the increase of the conversion rate between $Au_{0.98}Pd_{0.02}$ and $Pd_{0.04}Au_{0.96}$ on RCT-SiO₂ is unknown at this point.

A subsequent EDS investigation was performed to determine if Pd was oxidized or reduced (Figures S4 and S5). It is necessary to determine whether Pd is metallic or oxidized to link catalytic measurements with DFT analysis, as Pd and PdO do not have the same catalytic properties. The EDS map presented in Figure S4 shows that O could not be detected within the particles. Oxygen could be detected only with Si, so we conclude that only O is present in the SiO₂ support.

It has now been established that Pd remains metallic in AuPd particles. We have also shown that the particle's size is the same for all Au–Pd particles in this study and shown the presence of facets (mostly $\{111\}$ interfaces) on particles with low Pd concentrations. Sharp facets are dominant for Au_{0.98}Pd_{0.02}, Au_{0.96}Pd_{0.04}, and Au_{0.91}Pd_{0.09}. Au_{0.75}Pd_{0.25} was

excluded from the rest of the study, as the particles are not as faceted (with {111} interfaces) as the other three samples.

To elucidate the influence of the Pd content on the alkyne conversion rate, DFT analysis was performed. Acetylene, being the smallest alkyne molecule, was used as a model reactant for DFT calculations as it contains the most important functional group in 1-hexyne (i.e., triple bond) and helps reduce computational efforts. Additionally, the free energy profile of acetylene hydrogenation on isolated Pd atoms on Au-Pd surfaces is very similar to those derived for 1-hexyne hydrogenation on the same catalyst surface. 51,52 Hence, these calculations of acetylene were chosen to correlate the impact of the Au-Pd surface ensemble on triple bond hydrogenation reactivity. To simplify the study, Au-Pd {111} surfaces were considered for the calculations. This assumption was made as the Au-Pd particles with low Pd content are often icosahedrons, which have {111} interfaces. With an increased Pd concentration, the Au-Pd particles drift away from this model. Still, the image in Figure 2c and the Supporting Information indicate that Pd_{0.09}Au_{0.91} particles maintain mostly {111} facets, even though Pd atoms introduce some surface roughness in many particles. Thus, we also simplified Pd_{0.09}Au_{0.91} particles to a model with {111} facets, even though some surface roughness was sometimes observed. Additionally, exposure to high temperature favors convergence to a Wulff configuration with more faceted surfaces. Nevertheless, the link with experiments is limited to the Au_{0.98}Pd_{0.02}, $Au_{0.96}Pd_{0.04}$, and $Au_{0.91}Pd_{0.09}$ samples, as we have shown that Au_{0.75}Pd_{0.25} has a high surface roughness, and therefore, the simplification by considering only {111} facets cannot apply.

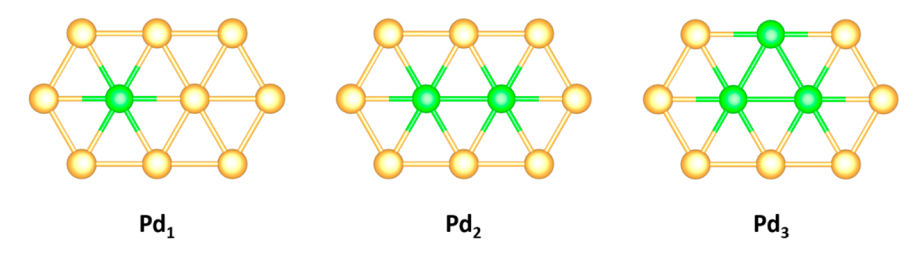


Figure 5. Schematic representation of Pd monomers (Pd_1) , Pd dimers (Pd_2) , and triangular Pd trimers (Pd_3) in the surface plane of Au(111). Color codes: Green (Pd); Gold (Au).

The {111} Au-Pd surfaces are modeled in terms of Pd monomers (isolated Pd atoms surrounded by Au atoms), Pd dimers, and triangular Pd trimers in the surface plane of a Au(111) slab (Figure 5). This modeling in terms of Pd monomers, dimers, and trimers has been used in a prior study, which combined DFT and X-ray absorption spectroscopy (XAS) analysis of the same Au-Pd particles.⁵³

The distribution of Pd monomers, dimers, and trimers can also be shown by a statistical model based on a binomial distribution (Table 1). If the Pd concentration increases, the numbers of Pd dimers and Pd trimers will become larger (see Table S6 and the Supporting Information for details).

Table 1. Probability of Finding Pd as Monomers, Dimers, and Trimers Based on the Binomial Distribution for the Surface Atoms, Assuming a Uniform Distribution of Pd

sample	% of Pd as monomers	% of Pd as dimers	% of Pd as trimers
$Au_{0.98}Pd_{0.02}$	88.6	10.8	0.6
$Au_{0.96}Pd_{0.04}$	78.4	19.6	2.0
$Au_{0.91}Pd_{0.09}$	56.8	33.6	8.4
$Au_{0.75}Pd_{0.25} \\$	17.8	35.6	29.6

The presence of Pd-rich islands observed in $Au_{0.91}Pd_{0.09}$ particles will further increase the probability of Pd dimers and trimers. In fact, EDS quantification showed that Pd islands in $Au_{0.91}Pd_{0.09}$ particles have a Pd concentration between 15% and 30%, making the probability of finding Pd dimers and trimers high. The analysis of the catalytic properties of monomers, dimers, and trimers will give us the key to determining why some concentrations of Pd lead to better activity. If a specific type of configuration (monomer, dimer, or trimer) is more active than the others, we can determine which concentration of Pd is more favorable.

Binding strengths of surface species on dilute alloys increase significantly with increasing Pd ensemble sizes (Table 2). On Pd₁, the adsorption free energy of acetylene is the smallest

Table 2. Adsorption and Reaction Free Energies of Various Species on Pd₁, Pd₂, and Pd₃ at T = 363 K, $P(H_2) = 0.2$ bar, $P(C_2H_2) = 0.01$ bar, and $P(C_2H_4) = P(C_2H_6) = 0.001$ bar^a

	Pd_1	Pd_2	Pd_3
$G_{ads}(C_2H_2)$	-0.05 eV	−0.37 eV	−1.03 eV
$G_{ads}(C_2H_4)$	0.19 eV	0.09 eV	−0.06 eV
G(2H)	0.35 eV	0.11 eV	−0.24 eV
$G(C_2H_3)$	−0.50 eV	−0.81 eV	−1.20 eV
$G(C_2H_5)$	−1.74 eV	−1.93 eV	-2.04 eV

^aFree energy values used gaseous H_2 and C_2H_2 as references, and the specific equations are given in the Supporting Information.

among the three different Pd ensembles, with the value being -0.05 eV under the studied condition. This small magnitude prevents the catalyst surface from being completely covered by acetylene and leaves a portion of the active sites vacant for H₂ activation. As the binding strength of acetylene generally outcompetes that of atomic H, the blocking of the active sites would only make H₂ activation more difficult on larger Pd ensembles, despite the stronger binding of atomic H and hence a smaller H₂ dissociation barrier on them. The adsorption free energies of ethylene also follow this identical pattern, with the binding strength being the weakest on Pd₁ and the strongest on Pd₃ (Table 2). On Pd₁ and Pd₂, the adsorption free energies of ethylene are positive, indicating the tendency to desorb. However, desorption of ethylene is slightly unfavorable on Pd₃ as designated by the negative value, which would hamper ethylene production. The free energy values of the reaction intermediates additionally mirror the same trend. Complete free energy profiles constructed under standard-state pressures for the three ensembles are provided in Figures S6 and S13, and the effect of the binding strength will be explored in more detail in the microkinetic simulations.

Microkinetic simulations were performed to shed light on the reaction rates and the rate- and selectivity-determining steps in the convoluted reaction mechanisms. The hydrogenation pathway starts with acetylene adsorption on one vacant Pdn active site and H2 activation on another Pdn active site of the alloy surface. Following the H₂ dissociation, one of the H atoms will migrate to the acetylene adsorption site and hydrogenate the molecule to chemisorbed ethylenyl ($C_2H_3^*$). Subsequent hydrogenation steps occur similarly, and the H migration event is assumed to take place every time a C-H bond is formed. C₂H₄* can desorb or be further hydrogenated. This reaction pathway is termed the regular pathway (Figure 6). In addition, two more reaction pathways were included exclusively for Pd₃, considering its larger ensemble size: (1) H₂ dissociation on the acetylene/ethylene adsorption site followed by C-H bond formation (no-migration pathway) and (2) adsorption of an acetylene/ethylene molecule on the Pd₃ ensemble where a H atom already resides on the Pd₃ fcc hollow site ([H³ - Pd₃]) and, subsequently, hydrogenation takes place (special pathway) (Figure 6).

Then, the reaction rates and degree of rate controls (DRCs) were calculated and are listed in Figure 7. The rate of acetylene hydrogenation on Pd monomers (Pd₁) is much higher than those on larger Pd ensembles (Figure 7a–c). The difference in the reaction rates among the three Pd ensembles is a consequence of the different adsorbate binding strengths. On Pd monomers, the binding of the reactant, acetylene, is weak with the adsorption free energy being -0.05 eV at T = 363 K (Table 2). As mentioned, this weak binding results in the active sites being only partially occupied by acetylene, which

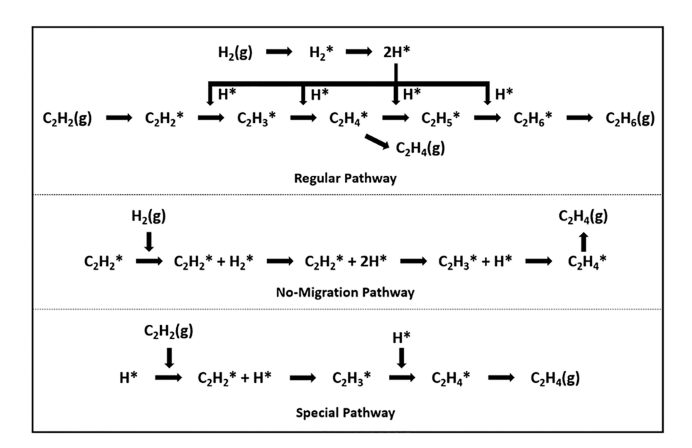


Figure 6. Schematic representation of the regular pathway, where acetylene adsorbs on one Pd_n site, H_2 adsorbs and dissociates on another Pd_n site, and H migrates over Au to reach the adsorbed acetylene and perform the successive hydrogenation steps; the nomigration pathway where for Pd_3 acetylene adsorbs on one Pd_3 site and H_2 subsequently adsorbs and dissociates on the same $Pd_3-C_2H_2^*$ site; the special pathway where acetylene adsorbs on a Pd_3 site occupied by one H adatom (noted ($[H^3-Pd_3]$). For simplicity, only the first half of the hydrogenation reaction ($C_2H_2 \rightarrow C_2H_4$) is shown in the latter two pathways as the second half ($C_2H_4 \rightarrow C_2H_6$) follows the same pattern. An asterisk indicates the surface species.

leaves some Pd_1 sites vacant for H_2 activation. Indeed, microkinetic simulation shows that acetylene coverage starts to decrease at T=323 K due to the entropy penalty, rendering the catalyst surface partly bare (Figure S14a). Notably, the production rate of ethylene also begins to increase at the same temperature. To better understand the rate-limiting steps in

acetylene hydrogenation on Pd₁, degree of rate control (DRC) calculations of the transition states were performed (Figure 7d-f). It is shown that H₂ dissociation is the most ratecontrolling step with a minor contribution from atomic H migration and C₂H₃ formation in the temperature range studied. The observation that H₂ molecular dissociation is the most rate-controlling step is also consistent with the weak binding of H species on Pd₁. For weak binding, the transition state for H2 dissociation is not well-stabilized, resulting in a large free energy barrier of 0.62 eV. It is noted that the apparent activation energy for acetylene hydrogenation drops from approximately 1.06 eV at T = 323 K to 0.73 eV at T =373 K (Figure S15). According to Mao and Campbell, the apparent activation energy (E_{app}) can be interpreted as the sum of the enthalpies of all transition states and surface intermediates weighed by their respective DRCs. 54 Hence, the decrease in $E_{\rm app}$ observed here is attributed to the lower DRC of the H₂ dissociation transition state (which has a positive enthalpy value) and the higher DRCs of the transition state for acetylene hydrogenation and the surface intermediate C₂H₂ across this temperature range (both of which possess negative enthalpy values) (see Figures 7 and S15).

Microkinetic simulations demonstrate that the reaction rate on Pd_2 is approximately one-tenth of that on Pd_1 (Figure 7b). This low reaction rate is a direct consequence of the strong binding of acetylene, of which the adsorption free energy is -0.37 eV at T=363 K (Table 2). This strong binding expels any H_2 molecules from the Pd active sites, rendering H_2 activation either impossible on occupied Pd ensembles or difficult on Au domains. Evidence from surface coverage and DRC analysis support this claim and are consistent with the free-energy-based analysis. It is shown that all of the Pd_2 active

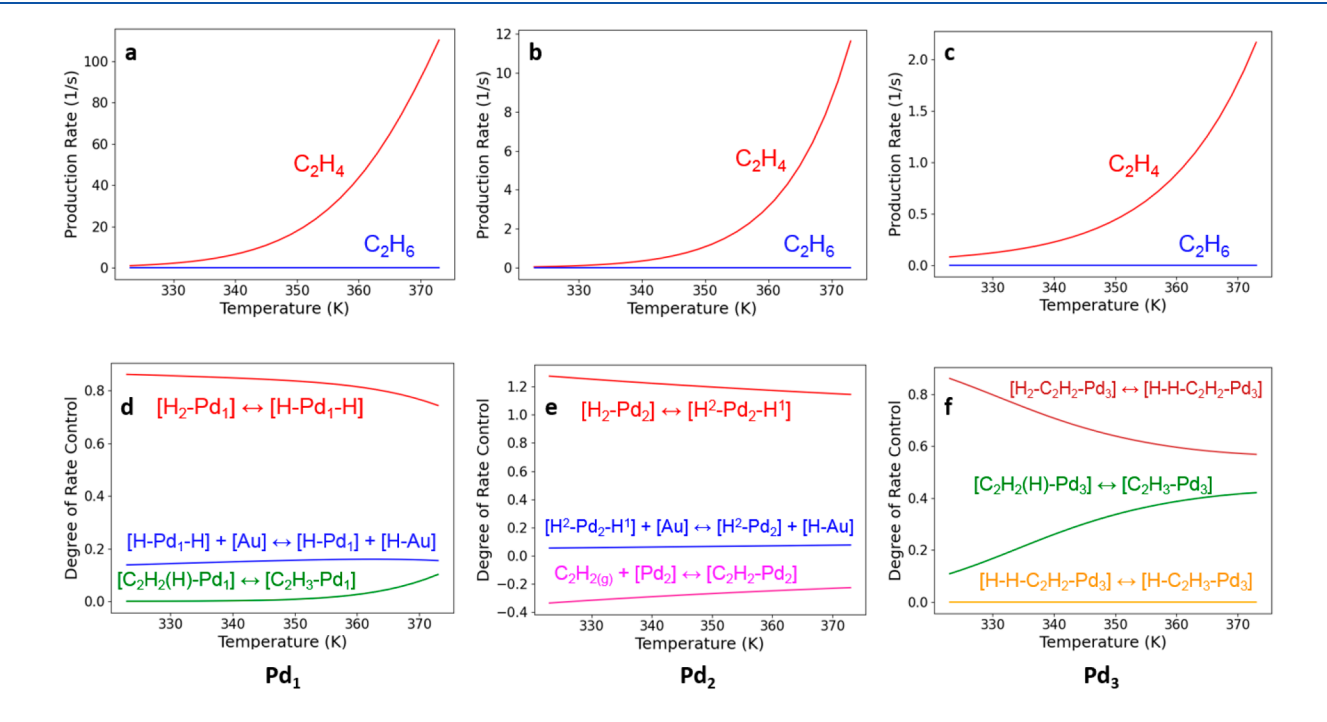


Figure 7. Reaction rates (a-c) and degree of rate controls (DRCs) of transition states (d-f) for acetylene hydrogenation on Pd_1 (a, d), Pd_2 (b, e), and Pd_3 (c, f) calculated using microkinetic simulations. Hydrocarbon coadsorbing with an H atom on a Pd ensemble in the regular pathway is denoted as $[C_2H_x(H)-Pd_y]$. Note that $[H-C_2H_3-Pd_3]$ also represents the coadsorption of C_2H_3 with an H atom, but its configuration differs from that in the regular pathway (see Figure S18). The number superscripted next to H in (e) is the coordination number of the H atom with the Pd atoms in the absence of any hydrocarbon. Only elementary steps with significant DRCs are shown in (d-f). The calculations were performed at $P(C_2H_2) = 0.01$ bar, $P(H_2) = 0.2$ bar, $P(C_2H_4) = 0.001$ bar, and $P(C_2H_6) = 0.001$ bar.

sites are solely occupied by acetylene in the entire temperature range studied (Figure S14b). Acetylene adsorption is also demonstrated to be negatively rate-controlling, meaning that if acetylene adsorption becomes more stabilizing, then the reaction rate would be even lower (Figure 7e). From an alternative perspective, since all active Pd sites are occupied by acetylene, H₂ dissociation becomes very positively ratedetermining on Pd2. Additionally, the apparent activation energy for this hydrogenation reaction on Pd2 remains constant at 1.16 eV (Figure S16). This value is very consistent with the enthalpy value of C₂H₂ on the catalyst surface weighed by its DRC of -1 (Figure S16), which further supports the claim that C2H2 poisons the active sites and renders the catalyst less active. Note that, although the transition state of H₂ dissociation has a large and positive DRC value, it has no impact on the $E_{\rm app}$ calculation, as the relative enthalpy value of this transition state is roughly equal to 0.

Pd₃ has the lowest reactivity for acetylene hydrogenation among the three Pd ensembles, with the reaction rate being approximately 2% that of Pd₁ (Figure 7c). Among all elementary steps, the most rate-controlling one is found to be the dissociation of H₂ on the same Pd₃ site, where an acetylene molecule already resides. Additionally, the hydrogenation of acetylene to form ethylenyl is also somewhat rate-controlled (Figure 7f). DRC of surface intermediates and apparent activation energy for acetylene hydrogenation on Pd₃ calculated using microkinetic simulations are provided in Figure S17. Since the reaction network on Pd₃ is convoluted, building a reaction scheme would be necessary to gain insight into these observations.

Now, one can interpret the reaction rates for Pd₁, Pd₂, and Pd₃ to explain the changes in activity shown in Figure 1. Pd₁ sites are more active than Pd2 sites, which are more active than Pd₃ sites. Au_{0.91}Pd_{0.09} has more Pd₂ and Pd₃ sites than Au_{0.96}Pd_{0.04} and fewer Pd₁ sites, based on the binomial distribution, as shown in Table 2. This explains why Au_{0.91}Pd_{0.09} is less active than Au_{0.96}Pd_{0.04} per gram of Pd. However, there seems to be a contradiction for the low activity of Au_{0.98}Pd_{0.02} (rich in Pd₁) compared to Au_{0.96}Pd_{0.04}. We hypothesize that Pd can more easily segregate on the surface of Au-Pd particles if the Pd concentration is high. Adding more Pd atoms to the Au particles increases the number of defects and voids that can facilitate the segregation of Pd to the surface after calcination. This is supported by the EDS data shown in Figures 3 and 4, where Pd islands segregated to the surface are visible for Au-Pd particles with high Pd concentration. Thus, Au_{0.96}Pd_{0.04} appears to benefit from two factors: A high concentration of active Pd1 sites was combined with Pd segregation to the surface. These two factors cannot be found together in $Au_{0.98}Pd_{0.02}$ and $Au_{0.91}Pd_{0.09}$.

Acetylene hydrogenation on Pd_3 involves three parallel reaction pathways, as shown in Figure S18. At steady state, instead of adsorbing acetylene on a bare Pd_3 site, the reaction starts with acetylene adsorption on $[H^3-Pd_3]$. Given that C_2H_2 on the Pd_3 hollow site is more stable than the H atom on the same site, the surface species undergo a configurational transformation to reach this new adsorption state $[C_2H_2(H)-Pd_3]$. The reaction then proceeds via a regular pathway in which an H atom is drawn to the hydrocarbon each time a C-H bond is created. Once ethylene is formed on the catalyst surface, most of it will desorb into the gas phase directly under the studied condition. The rest will participate in the regular pathway again to reach the state of ethylene coadsorbing with

another H atom $[C_2H_4(H)-Pd_3]$. It is more stable to put the H atom on the Pd₃ hollow site and C_2H_4 on the Pd₁ top site (as in the special pathway $[C_2H_4(H)-Pd_3-SP]$) than to put the configuration where C_2H_4 is on the Pd-Pd bridge site and the H atom is on the Au_1-Pd_2 hollow site (as in the regular pathway $[C_2H_4(H)-Pd_3]$). Additionally, $[C_2H_4(H)-Pd_3-SP]$ also lies lower in free energy than ethyl. Hence, $[C_2H_4(H)-Pd_3]$ in the regular pathway will transform into the special pathway configuration $[C_2H_4(H)-Pd_3-SP]$. Ethylene desorption could subsequently occur, leaving the H atom on the Pd₃ hollow site.

However, the dissociation of H₂ in the presence of acetylene as in the no-migration pathway is the most rate-controlling step on Pd₃ (Figure 7f). The no-migration pathway begins with the H_2 adsorption on $[C_2H_2-Pd_3]$, followed by dissociation to reach the state where C₂H₂ coadsorbs with two H atoms. Since the Pd3 hollow site is occupied by the acetylene molecule, the dissociation must take place on the Au₂-Pd₁ hollow site. Hence, the H₂ dissociation free energy barrier in the nomigration pathway is much higher than that on a bare active site (0.85 eV for the former and 0.16 eV for the latter under standard-state pressures). Following the dissociation, one of the two H atoms can either attach to the acetylene molecule to form C₂H₃ or migrate away from the Pd₃ ensemble for hydrogenation on a second active site. Microkinetic simulations demonstrate that migration is more favorable, and the surface species left behind would transform into the coadsorption configuration in the regular pathway. The nomigration pathway is not the most active pathway in acetylene hydrogenation on Pd3 as indicated by its reaction rate of 0.31 s^{-1} at T = 363 K, which is lower than the overall reaction rate of 1.1 s⁻¹ at the same temperature. Yet, this pathway possesses the greatest positive degree of rate control. In other words, the overall reaction rate is most severely impacted by this elementary step of H₂ dissociation in the no-migration pathway. This pathway acts as an amplifier in the coupled reaction mechanism for enhancing the reaction rate.

To further support the claim that 1-hexyne and acetylene possess similar reaction kinetics in the hydrogenation reaction, full microkinetic modeling was conducted for the same reaction of 1-hexyne on the Pd1 ensemble as an illustration (Figure S19). It is shown that, under the same studied conditions, the production rate of 1-hexene from 1-hexyne is very similar to that of ethylene from acetylene, with the difference being smaller than a factor of 2. Additionally, hexane is also not produced in the process, and H2 dissociation remains the most rate-controlling transition state based on DRC analysis (Figure S19). These observations are highly consistent with those seen for acetylene hydrogenation on the same Pd₁ ensemble. Since H₂ dissociation is the most ratelimiting process in the hydrogenation reactions on all three Pd ensembles, the reaction kinetics do not depend on the alkyne molecule that one is using. Hence, the findings derived for the smaller alkyne molecule, acetylene, can be confidently extrapolated to the larger molecule, 1-hexyne. This result justifies our choice of using acetylene as a model reactant for this study.

We have hence demonstrated the origin of the high activity for alkyne hydrogenation with dilute Pd in Au particles. We also explain why the selectivity is high for the three samples. All three Pd ensembles $(Pd_1,\ Pd_2,\ and\ Pd_3)$ were shown to produce only ethylene, which is the desired product, in the temperature range studied, i.e., corresponding to 100%

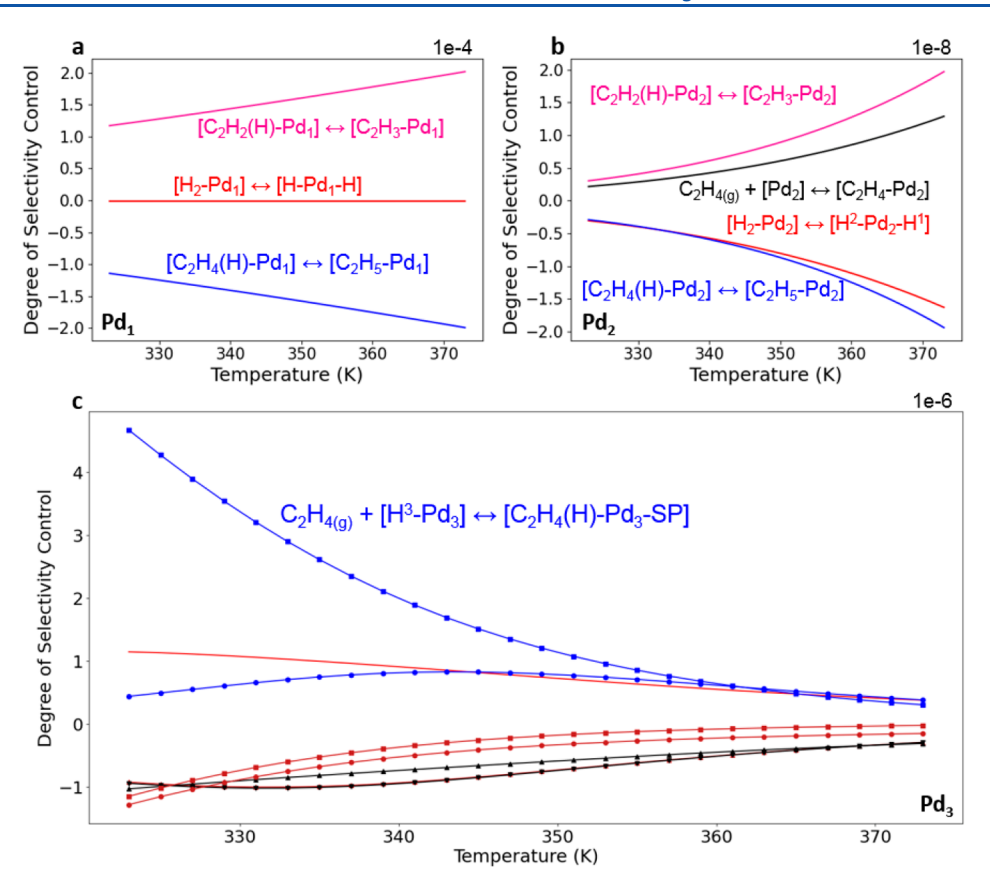


Figure 8. Degree of selectivity controls (DSCs) of transition states for acetylene hydrogenation on (a) Pd_1 , (b) Pd_2 , and (c) Pd_3 calculated using microkinetic simulations. On Pd_3 , steps with positive DSCs include $C_2H_{4(g)} + [H^3 - Pd_3] \rightleftharpoons [C_2H_4(H) - Pd_3 - SP]$ (blue square), $C_2H_{4(g)} + [Pd_3] \rightleftharpoons [C_2H_4 - Pd_3]$ (blue circle), and $[C_2H_2(H) - Pd_3] \rightleftharpoons [C_2H_3 - Pd_3]$ (red curve). Steps with negative DSCs, on the other hand, include $[H_2 - C_2H_2 - Pd_3] \rightleftharpoons [H - H - C_2H_2 - Pd_3]$ (black triangle up), $[H_2 - C_2H_4 - Pd_3] \rightleftharpoons [H - H - C_2H_4 - Pd_3]$ (black triangle down), $[C_2H_4(H) - Pd_3] \rightleftharpoons [C_2H_5 - Pd_3]$ (dark red square), and $[H - H - C_2H_4 - Pd_3] \rightleftharpoons [C_2H_5(H) - Pd_3]$ (dark red triangle up). Note that the curves of H_2 dissociation in the presence of ethylene (black triangle down) and the subsequent C - H bond formation (dark red triangle up) overlap in (c). For simplicity, elementary steps with negligible DSCs are excluded from the results. The calculation was evaluated at $P(C_2H_2) = 0.01$ bar, $P(H_2) = 0.2$ bar, $P(C_2H_4) = 0.001$ bar, and $P(C_2H_6) = 0.001$ bar.

selectivity. To investigate the reasons behind this high selectivity (which was experimentally observed in Figure 1), degree of selectivity control (DSC) calculations of the transition states were carried out (Figure 8). The selectivity here is defined as the ratio of the ethylene formation rate to the acetylene consumption rate. It is broadly accepted that easy desorption of the partially hydrogenated product is the key to enhancing selectivity. However, in the case of Pd₁, the high selectivity is mainly attributed to the easy hydrogenation of acetylene to form ethylenyl. If more ethylenyl is formed, then more ethylene could subsequently be formed, too, especially when the second hydrogenation step has a smaller free energy barrier. Ethylene hydrogenation, on the other hand, has a negative degree of selectivity control. The negative value is easily understood by the fact that more of the desired product will be consumed if this ethylene hydrogenation step is made easier, which would shrink the numerator in the definition aforementioned and hence the selectivity.

In the case of Pd₂, the high selectivity is a consequence of the ethylene desorption in addition to the first acetylene hydrogenation step. The reasoning behind ethylene desorption to enhance selectivity is straightforward, as once desorbed, ethylene would not stay on the catalyst surface for further hydrogenation to form the undesired product ethane. On the same catalyst surface, H₂ dissociation is found to negatively impact the selectivity for ethylene formation, in addition to ethylene hydrogenation. When $\rm H_2$ dissociation is made easier, atomic H would become more readily available. These H atoms could subsequently hydrogenate more ethylene molecules, which in turn, reduces the ethylene formation and selectivity.

On Pd₃, the selectivity for ethylene formation is controlled by several elementary steps. Among them, the DSC of C₂H₄ desorption from the catalyst surface with an H atom on the Pd₃ hollow site (blue square in Figure 8c, special pathway) is the most positive. This positivity suggests that, if C₂H₄ desorption is made easier, the selectivity would be enhanced, as there are fewer ethylene molecules on the surface for further hydrogenation. The same also applies to the desorption of C₂H₄ in the absence of the H atom (blue circle in Figure 8c, regular pathway), which has a positive DSC but a smaller magnitude. In addition, hydrogenation of C2H2 to form C2H3 in the regular pathway also has a positive DSC as it will augment the production of ethylene and hence increase the selectivity. On the other hand, steps with negative DSCs include the hydrogenation of C₂H₄ in the regular pathway (dark red circle in Figure 8c), special pathway (dark red square in Figure 8c), and the no-migration pathway (dark red triangle up in Figure 8c). These elementary steps consume the desired product C_2H_4 and encourage unwanted C_2H_6 generation. The

selectivity for ethylene formation will hence decrease if these steps are able to proceed with lower free energy barriers. Additionally, H_2 dissociation in the presence of C_2H_2 and C_2H_4 as in the no-migration pathway also has a negative DSC (black curves in Figure 8c). This is justified by the fact that, if H_2 dissociation becomes more facile, atomic H will become more readily available, which could participate in the overhydrogenation reaction to form the undesired product ethane.

CONCLUSION

To conclude, the STEM analysis showed that the surface of the particles has mostly {111} facets in Au_{0.98}Pd_{0.02}, Au_{0.96}Pd_{0.04}, and Au_{0.91}Pd_{0.09} particles. It demonstrates that Au–Pd particles with higher Pd concentrations (in the considered regime, where Pd is diluted) show substantial segregation of Pd to the surface. In parallel, the DFT analysis shows the high activity of isolated Pd atoms (Pd₁) compared to small aggregated Pd ensembles on the surface (Pd2 and Pd3). Thus, an optimum Pd concentration exists to strike a balance between a high concentration of Pd monomers and a high segregation of Pd atoms to the surface. Au_{0.96}Pd_{0.04} is the most active combination, as the low concentration of Pd (4%) is rich in Pd1 sites, and the Pd concentration is high enough to facilitate the segregation of Pd to the surface. The DFT analysis also explains a previously reported experimental result showing the high selectivity of Au-Pd particles with a low Pd concentration. Thus, combining STEM, DFT, and catalytic testing is a powerful approach to understanding and improving innovative catalysts and can be expanded to many complex systems.55-5

ASSOCIATED CONTENT

Supporting Information

The Supporting Information is available free of charge at https://pubs.acs.org/doi/10.1021/acsanm.3c04278.

Additional STEM images, EELS, EDS data, description of reaction pathways, degree of rate control (DRC), reaction rates, and elementary steps of microkinetics simulations (PDF)

AUTHOR INFORMATION

Corresponding Author

Eric A. Stach — Department of Materials Science and Engineering, University of Pennsylvania, Philadelphia, Pennsylvania 19104, United States; orcid.org/0000-0002-3366-2153; Email: stach@seas.upenn.edu

Authors

Alexandre C. Foucher – Department of Materials Science and Engineering, University of Pennsylvania, Philadelphia, Pennsylvania 19104, United States; orcid.org/0000-0001-5042-4002

Hio Tong Ngan – Department of Chemical and Biomolecular Engineering, University of California, Los Angeles, California 90095, United States

Tanya Shirman – John A. Paulson School of Engineering and Applied Sciences, Harvard University, Cambridge, Massachusetts 02138, United States

Amanda Filie – John A. Paulson School of Engineering and Applied Sciences, Harvard University, Cambridge, Massachusetts 02138, United States Kaining Duanmu – Department of Chemical and Biomolecular Engineering, University of California, Los Angeles, California 90095, United States

Michael Aizenberg — John A. Paulson School of Engineering and Applied Sciences, Harvard University, Cambridge, Massachusetts 02138, United States; orcid.org/0000-0002-2901-7012

Robert J. Madix — John A. Paulson School of Engineering and Applied Sciences, Harvard University, Cambridge, Massachusetts 02138, United States; orcid.org/0000-0002-3132-2382

Cynthia M. Friend — John A. Paulson School of Engineering and Applied Sciences and Department of Chemistry and Chemical Biology, Harvard University, Cambridge, Massachusetts 02138, United States; orcid.org/0000-0002-8673-9046

Joanna Aizenberg — John A. Paulson School of Engineering and Applied Sciences and Department of Chemistry and Chemical Biology, Harvard University, Cambridge, Massachusetts 02138, United States; orcid.org/0000-0002-2343-8705

Philippe Sautet — Department of Chemical and Biomolecular Engineering and Department of Chemistry and Biochemistry, University of California, Los Angeles, California 90095, United States; occid.org/0000-0002-8444-3348

Complete contact information is available at: https://pubs.acs.org/10.1021/acsanm.3c04278

Author Contributions

OA.C.F. and H.T.N. contributed equally to this work.

Notes

The authors declare no competing financial interest.

ACKNOWLEDGMENTS

This work was supported as part of the Integrated Mesoscale Architectures for Sustainable Catalysis (IMASC), an Energy Frontier Research Center funded by the U.S. Department of Energy, Office of Science, Basic Energy Sciences under Award #DE-SC0012573. Experiments were also carried out at the Singh Center for Nanotechnology at the University of Pennsylvania, supported by the National Science Foundation (NSF) National Nanotechnology Coordinated Infrastructure Program grant NNCI-1542153. Additional support to the Nanoscale Characterization Facility at the Singh Center has been provided by the Laboratory for Research on the Structure of Matter (MRSEC) supported by the National Science Foundation (DMR-1720530). The DFT calculations used computational and storage services associated with the Hoffman2 cluster at the UCLA Institute for Digital Research and Education (IDRE), the National Energy Research Scientific Computing Center (NERSC) of the U.S. Department of Energy, and the Bridges-2 cluster at the Pittsburgh Supercomputing Center. The authors thank Dr. George Yan for helpful discussions.

REFERENCES

(1) Qi, Y.; Shao, X.; Wang, B.; Li, D.; Ling, L.; Zhang, R. C2H2 Semi-Hydrogenation on the Pdshell@Mcore (M = Cu, Ag, Au) Alloy Catalysts: The Influence of Shell Pd Ensemble Form on the Catalytic Activity and Selectivity. *Chem. Eng. Sci.* **2021**, 245, 116941.

(2) Wang, Y.; Wang, B.; Ling, L.; Zhang, R.; Fan, M. Probe into the Effects of Surface Composition and Ensemble Effect of Active Sites on

- the Catalytic Performance of C_2H_2 Semi-Hydrogenation over the Pd-Ag Bimetallic Catalysts. *Chem. Eng. Sci.* **2020**, 218, 115549.
- (3) Ma, C. Y.; Dou, B. J.; Li, J. J.; Cheng, J.; Hu, Q.; Hao, Z. P.; Qiao, S. Z. Catalytic Oxidation of Benzyl Alcohol on Au or Au-Pd Nanoparticles Confined in Mesoporous Silica. *Appl. Catal. B Environ.* **2009**, 92, 202–208.
- (4) Kortlever, R.; Peters, I.; Balemans, C.; Kas, R.; Kwon, Y.; Mul, G.; Koper, M. T. M. Palladium-Gold Catalyst for the Electrochemical Reduction of CO₂ to C1-C5 Hydrocarbons. *Chem. Commun.* **2016**, 52, 10229–10232.
- (5) Pizzutilo, E.; Freakley, S. J.; Cherevko, S.; Venkatesan, S.; Hutchings, G. J.; Liebscher, C. H.; Dehm, G.; Mayrhofer, K. J. J. Gold-Palladium Bimetallic Catalyst Stability: Consequences for Hydrogen Peroxide Selectivity. *ACS Catal.* **2017**, *7*, 5699–5705.
- (6) Luneau, M.; Shirman, T.; Foucher, A. C.; Duanmu, K.; Verbart, D. M. A.; Sautet, P.; Stach, E. A.; Aizenberg, J.; Madix, R. J.; Friend, C. M. Achieving High Selectivity for Alkyne Hydrogenation at High Conversions with Compositionally Optimized PdAu Nanoparticle Catalysts in Raspberry Colloid-Templated SiO₂. ACS Catal. **2020**, 10, 441–450.
- (7) McCue, A. J.; Baker, R. T.; Anderson, J. A. Acetylene Hydrogenation over Structured Au-Pd Catalysts. *Faraday Discuss.* **2016**, *188* (0), 499–523.
- (8) Choudhary, T. V.; Sivadinarayana, C.; Datye, A. K.; Kumar, D.; Goodman, D. W. Acetylene Hydrogenation on Au-Based Catalysts. *Catal. Lett.* **2003**, *86*, 1–8.
- (9) Liu, J.; Shan, J.; Lucci, F. R.; Cao, S.; Sykes, E. C. H.; Flytzani-Stephanopoulos, M. Palladium-Gold Single Atom Alloy Catalysts for Liquid Phase Selective Hydrogenation of 1-Hexyne. *Catal. Sci. Technol.* **2017**, *7*, 4276–4284.
- (10) Ding, Y.; Fan, F.; Tian, Z.; Wang, Z. L. Atomic Structure of Au-Pd Bimetallic Alloyed Nanoparticles. *J. Am. Chem. Soc.* **2010**, *132*, 12480–12486.
- (11) Vilé, G.; Albani, D.; Almora-Barrios, N.; López, N.; Pérez-Ramírez, J. Advances in the Design of Nanostructured Catalysts for Selective Hydrogenation. *ChemCatChem.* **2016**, *8*, 21–33.
- (12) Shirman, T.; Toops, T. J.; Shirman, E.; Shneidman, A. V.; Liu, S.; Gurkin, K.; Alvarenga, J.; Lewandowski, M. P.; Aizenberg, M.; Aizenberg, J. Raspberry Colloid-Templated Approach for the Synthesis of Palladium-Based Oxidation Catalysts with Enhanced Hydrothermal Stability and Low-Temperature Activity. *Catal. Today* **2021**, *360*, 241–251.
- (13) Filie, A.; Shirman, T.; Aizenberg, M.; Aizenberg, J.; Friend, C. M.; Madix, R. J. The Dynamic Behavior of Dilute Metallic Alloy Pd x Au 1–x /SiO 2 Raspberry Colloid Templated Catalysts under CO Oxidation. *Catal. Sci. Technol.* **2021**, *11*, 4072–4082.
- (14) Shirman, T.; Lattimer, J.; Luneau, M.; Shirman, E.; Reece, C.; Aizenberg, M.; Madix, R. J.; Aizenberg, J.; Friend, C. M. New Architectures for Designed Catalysts: Selective Oxidation Using AgAu Nanoparticles on Colloid-Templated Silica. *Chem. A Eur. J.* **2018**, *24*, 1833–1837.
- (15) Filie, A.; Shirman, T.; Foucher, A. C.; Stach, E. A.; Aizenberg, M.; Aizenberg, J.; Friend, C. M.; Madix, R. J. Dilute Pd-in-Au Alloy RCT-SiO₂ Catalysts for Enhanced Oxidative Methanol Coupling. *J. Catal.* **2021**, *404*, 943–953.
- (16) Marcella, N.; Liu, Y.; Timoshenko, J.; Guan, E.; Luneau, M.; Shirman, T.; Plonka, A. M.; Van Der Hoeven, J. E. S.; Aizenberg, J.; Friend, C. M.; Frenkel, A. I. Neural Network Assisted Analysis of Bimetallic Nanocatalysts Using X-Ray Absorption near Edge Structure Spectroscopy. *Phys. Chem. Chem. Phys.* **2020**, 22, 18902–18910.
- (17) Luneau, M.; Shirman, T.; Filie, A.; Timoshenko, J.; Chen, W.; Trimpalis, A.; Flytzani-Stephanopoulos, M.; Kaxiras, E.; Frenkel, A. I.; Aizenberg, J.; Friend, C. M.; Madix, R. J. Dilute Pd/Au Alloy Nanoparticles Embedded in Colloid-Templated Porous SiO2: Stable Au-Based Oxidation Catalysts. *Chem. Mater.* **2019**. *31*, 5759–5768.
- (18) van der Hoeven, J. E. S.; Kramer, S.; Dussi, S.; Shirman, T.; Park, K.-C. K.; Rycroft, C. H.; Bell, D. C.; Friend, C. M.; Aizenberg, J. On the Origin of Sinter-Resistance and Catalyst Accessibility in

- Raspberry-Colloid-Templated Catalyst Design. Adv. Funct. Mater. 2021, 31, 2106876.
- (19) Zhang, N.; Qiu, Y.; Sun, H.; Hao, J.; Chen, J.; Xi, J.; Liu, J.; He, B.; Bai, Z. W. Substrate-Assisted Encapsulation of Pd-Fe Bimetal Nanoparticles on Functionalized Silica Nanotubes for Catalytic Hydrogenation of Nitroarenes and Azo Dyes. *ACS Appl. Nano Mater.* **2021**, *4*, 5854–5863.
- (20) Luneau, M.; Guan, E.; Chen, W.; Foucher, A. C.; Marcella, N.; Shirman, T.; Verbart, D. M. A.; Aizenberg, J.; Aizenberg, M.; Stach, E. A.; Madix, R. J.; Frenkel, A. I.; Friend, C. M. Enhancing Catalytic Performance of Dilute Metal Alloy Nanomaterials. *Commun. Chem.* **2020**. *3*. 1–9.
- (21) Shi, W.; Sahoo, Y.; Swihart, M. T.; Prasad, P. N. Gold Nanoshells on Polystyrene Cores for Control of Surface Plasmon Resonance. *Langmuir* **2005**, *21*, 1610–1617.
- (22) Timoshenko, J.; Wrasman, C. J.; Luneau, M.; Shirman, T.; Cargnello, M.; Bare, S. R.; Aizenberg, J.; Friend, C. M.; Frenkel, A. I. Probing Atomic Distributions in Mono- and Bimetallic Nanoparticles by Supervised Machine Learning. *Nano Lett.* **2019**, *19*, 520–529.
- (23) Liu, M.; Guyot-Sionnest, P. Mechanism of Silver(I)-Assisted Growth of Gold Nanorods and Bipyramids. *J. Phys. Chem. B* **2005**, 109, 22192–22200.
- (24) Scott, M. C.; Chen, C. C.; Mecklenburg, M.; Zhu, C.; Xu, R.; Ercius, P.; Dahmen, U.; Regan, B. C.; Miao, J. Electron Tomography at 2.4-Ångström Resolution. *Nature* **2012**, 483, 444–447.
- (25) Zhang, C.; Zhang, J.; Han, B.; Zhao, Y.; Li, W. Synthesis of Icosahedral Gold Particles by a Simple and Mild Route. *Green Chem.* **2008**, *10*, 1094–1098.
- (26) Kwon, K.; Lee, K. Y.; Lee, Y. W.; Kim, M.; Heo, J.; Ahn, S. J.; Han, S. W. Controlled Synthesis of Icosahedral Gold Nanoparticles and Their Surface-Enhanced Raman Scattering Property. *J. Phys. Chem. C* **2007**, *111*, 1161–1165.
- (27) Zaera, F. The Surface Chemistry of Metal-Based Hydrogenation Catalysis. ACS Catal. 2017, 7, 4947–4967.
- (28) Lei, D.; Yu, K.; Li, M. R.; Wang, Y.; Wang, Q.; Liu, T.; Liu, P.; Lou, L. L.; Wang, G.; Liu, S. Facet Effect of Single-Crystalline Pd Nanocrystals for Aerobic Oxidation of 5-Hydroxymethyl-2-Furfural. *ACS Catal.* **2017**, *7*, 421–432.
- (29) De Gregorio, G. L.; Burdyny, T.; Loiudice, A.; Iyengar, P.; Smith, W. A.; Buonsanti, R. Facet-Dependent Selectivity of Cu Catalysts in Electrochemical CO2 Reduction at Commercially Viable Current Densities. ACS Catal. 2020, 10, 4854–4862.
- (30) Bu, L.; Guo, S.; Zhang, X.; Shen, X.; Su, D.; Lu, G.; Zhu, X.; Yao, J.; Guo, J.; Huang, X. Surface Engineering of Hierarchical Platinum-Cobalt Nanowires for Efficient Electrocatalysis. *Nat. Commun.* **2016**, *7*, 1–10.
- (31) Guo, X.; Yates, J. T. Dependence of Effective Desorption Kinetic Parameters on Surface Coverage and Adsorption Temperature: CO on Pd(111). *J. Chem. Phys.* **1989**, *90*, *6761–6766*.
- (32) Guan, E.; Foucher, A. C.; Marcella, N.; Shirman, T.; Luneau, M.; Head, A. R.; Verbart, D. M. A.; Aizenberg, J.; Friend, C. M.; Stacchiola, D.; Stach, E. A.; Frenkel, A. I. New Role of Pd Hydride as a Sensor of Surface Pd Distributions in Pd—Au Catalysts. *ChemCatChem.* **2020**, *12*, 717—721.
- (33) Ngan, H. T.; Yan, G.; Van Der Hoeven, J. E. S.; Madix, R. J.; Friend, C. M.; Sautet, P. Hydrogen Dissociation Controls 1-Hexyne Selective Hydrogenation on Dilute Pd-in-Au Catalysts. *ACS Catal.* **2022**, *12*, 13321–13333.
- (34) Enhanced Catalytic Materials with Partially Embedded Catalytic Nanoparticles. US 11590483 B2, 2018.
- (35) van der Hoeven, J. E. S.; Ngan, H. T.; Taylor, A.; Eagan, N. M.; Aizenberg, J.; Sautet, P.; Madix, R. J.; Friend, C. M. Entropic Control of HD Exchange Rates over Dilute Pd-in-Au Alloy Nanoparticle Catalysts. ACS Catal. 2021, 11, 6971–6981.
- (36) Kresse, G. Ab Initio Molecular Dynamics for Liquid Metals. J. Non. Cryst. Solids 1995, 192–193, 222–229.
- (37) Kresse, G.; Hafner, J. *Ab Initio* Molecular-Dynamics Simulation of the Liquid-Metal—Amorphous-Semiconductor Transition in Germanium. *Phys. Rev. B* **1994**, 49, 14251.

- (38) Steinmann, S. N.; Corminboeuf, C. Comprehensive Benchmarking of a Density-Dependent Dispersion Correction. *J. Chem. Theory Comput.* **2011**, *7*, 3567–3577.
- (39) Perdew, J. P.; Burke, K.; Ernzerhof, M. Generalized Gradient Approximation Made Simple. *Phys. Rev. Lett.* **1996**, *77*, 3865.
- (40) Monkhorst, H. J.; Pack, J. D. Special Points for Brillouin-Zone Integrations. *Phys. Rev. B* **1976**, *13*, 5188.
- (41) Henkelman, G.; Uberuaga, B. P.; Jónsson, H. A Climbing Image Nudged Elastic Band Method for Finding Saddle Points and Minimum Energy Paths. *J. Chem. Phys.* **2000**, *113*, 9901.
- (42) Henkelman, G.; Jónsson, H. A Dimer Method for Finding Saddle Points on High Dimensional Potential Surfaces Using Only First Derivatives. *J. Chem. Phys.* **1999**, *111*, 7010.
- (43) Momma, K.; Izumi, F. VESTA 3 for Three-Dimensional Visualization of Crystal, Volumetric and Morphology Data. *J. Appl. Crystallogr.* **2011**, *44*, 1272–1276.
- (44) Campbell, C. T. The Degree of Rate Control: A Powerful Tool for Catalysis Research. *ACS Catal.* **2017**, *7*, 2770–2779.
- (45) Akbarzadeh, H.; Abbaspour, M.; Mehrjouei, E. Au@Pt and Pt@Au Nanoalloys in the Icosahedral and Cuboctahedral Structures: Which Is More Stable? *J. Mol. Liq.* **2017**, 242, 1002–1017.
- (46) Akbarzadeh, H.; Abbaspour, M.; Mehrjouei, E. Effect of Systematic Addition of the Third Component on the Melting Characteristics and Structural Evolution of Binary Alloy Nanoclusters. *J. Mol. Liq.* **2018**, 249, 412–419.
- (47) Foucher, A. C.; Owen, C. J.; Shirman, T.; Aizenberg, J.; Kozinsky, B.; Stach, E. A. Atomic-Scale STEM Analysis Shows Structural Changes of Au-Pd Nanoparticles in Various Gaseous Environments. J. Phys. Chem. C 2022, 126, 18047—18056.
- (48) Xin, H. L.; Alayoglu, S.; Tao, R.; Genc, A.; Wang, C. M.; Kovarik, L.; Stach, E. A.; Wang, L. W.; Salmeron, M.; Somorjai, G. A.; Zheng, H. Revealing the Atomic Restructuring of Pt-Co Nanoparticles. *Nano Lett.* **2014**, *14*, 3203–3207.
- (49) Liu, Z.; Xin, H.; Yu, Z.; Zhu, Y.; Zhang, J.; Mundy, J. A.; Muller, D. A.; Wagner, F. T. Atomic-Scale Compositional Mapping and 3-Dimensional Electron Microscopy of Dealloyed PtCo₃ Catalyst Nanoparticles with Spongy Multi-Core/Shell Structures. *J. Electrochem. Soc.* **2012**, *159* (9), F554–F559.
- (50) Guan, E.; Foucher, A. C.; Marcella, N.; Shirman, T.; Luneau, M.; Head, A. R.; Verbart, D. M. A.; Aizenberg, J.; Friend, C. M.; Stacchiola, D.; Stach, E. A.; Frenkel, A. I. New Role of Pd Hydride as a Sensor of Surface Pd Distributions in Pd—Au Catalysts. *ChemCatChem.* 2020, 12, 717—721.
- (51) Ngan, H. T.; Yan, G.; van der Hoeven, J. E. S.; Madix, R. J.; Friend, C. M.; Sautet, P. Hydrogen Dissociation Controls 1-Hexyne Selective Hydrogenation on Dilute Pd-in-Au Catalysts. *ACS Catal.* **2022**, *12*, 13321–13333.
- (52) Van Der Hoeven, J. E. S.; Ngan, H. T.; Yan, G.; Aizenberg, J.; Madix, R. J.; Sautet, P.; Friend, C. M. Unraveling 1-Hexene Hydrogenation over Dilute Pd-in-Au Alloys. *J. Phys. Chem. C* **2022**, 126 (37), 15710–15723.
- (53) Marcella, N.; Lim, J. S.; Płonka, A. M.; Yan, G.; Owen, C. J.; van der Hoeven, J. E. S.; Foucher, A. C.; Ngan, H. T.; Torrisi, S. B.; Marinkovic, N. S.; Stach, E. A.; Weaver, J. F.; Aizenberg, J.; Sautet, P.; Kozinsky, B.; Frenkel, A. I. Decoding Reactive Structures in Dilute Alloy Catalysts. *Nat. Commun.* 2022 131 2022, 13, 1–9.
- (54) Mao, Z.; Campbell, C. T. Apparent Activation Energies in Complex Reaction Mechanisms: A Simple Relationship via Degrees of Rate Control. *ACS Catal.* **2019**, *9*, 9465–9473.
- (55) Wang, D.; Xin, H. L.; Hovden, R.; Wang, H.; Yu, Y.; Muller, D. A.; DiSalvo, F. J.; Abruña, H. D. Structurally Ordered Intermetallic Platinum–Cobalt Core–Shell Nanoparticles with Enhanced Activity and Stability as Oxygen Reduction Electrocatalysts. *Nat. Mater.* **2013**, *12*, 81–87.
- (56) Zugic, B.; Wang, L.; Heine, C.; Zakharov, D. N.; Lechner, B. A. J.; Stach, E. A.; Biener, J.; Salmeron, M.; Madix, R. J.; Friend, C. M. Dynamic Restructuring Drives Catalytic Activity on Nanoporous Gold-Silver Alloy Catalysts. *Nat. Mater.* **2017**, *16*, 558–564.

(57) van der Hoeven, J. E. S.; Jelic, J.; Olthof, L. A.; Totarella, G.; van Dijk-Moes, R. J. A.; Krafft, J. M.; Louis, C.; Studt, F.; van Blaaderen, A.; de Jongh, P. E. Unlocking Synergy in Bimetallic Catalysts by Core—Shell Design. *Nat. Mater.* **2021**, *20*, 1216–1220.